



HAL
open science

Linear to turbulent Görtler instability transition

Jérémie Dagaut, M.E. Negretti, Guillaume Balarac, Christophe Brun

► **To cite this version:**

Jérémie Dagaut, M.E. Negretti, Guillaume Balarac, Christophe Brun. Linear to turbulent Görtler instability transition. *Physics of Fluids*, 2021, 33 (1), pp.014102. 10.1063/5.0033944 . hal-03124690

HAL Id: hal-03124690

<https://hal.science/hal-03124690>

Submitted on 8 Oct 2021

HAL is a multi-disciplinary open access archive for the deposit and dissemination of scientific research documents, whether they are published or not. The documents may come from teaching and research institutions in France or abroad, or from public or private research centers.

L'archive ouverte pluridisciplinaire **HAL**, est destinée au dépôt et à la diffusion de documents scientifiques de niveau recherche, publiés ou non, émanant des établissements d'enseignement et de recherche français ou étrangers, des laboratoires publics ou privés.

Linear to turbulent Görtler instability transition

J. Dagaut,¹ M.E. Negretti,^{1, a)} G. Balarac,^{1, 2} and C. Brun¹

¹⁾*Univ. Grenoble Alpes, CNRS, Grenoble INP, LEGI, 38000, Grenoble, France*

²⁾*Institut Univ. de France, 1 rue Descartes, 75231 Paris, France*

(Dated: 8 October 2021)

We present results from a high resolved Large Eddy Simulation of a freely developing Blasius profile over a concave boundary in a large spanwise domain. Due to the large initial Reynolds and Görtler numbers ($Re_{\theta,0} = 1170, G_{\theta,0} = 75$), we observe the onset of two dominant wavelengths, the first dominating in the linear/transition region, λ_1 , and the second dominating in the turbulent region, λ_2 . Extending previous linear stability analysis (LSA) to higher Görtler numbers and non-dimensional wavenumbers, both dominant wavelengths of the Görtler instability correspond to predictions of LSA, the latter comparable to laminar theory by replacing the kinematic viscosity with the turbulent viscosity in the definition of the Görtler number. The predicted spatial modes compare well with the computed profiles for both λ_1 and λ_2 . The skin friction coefficient C_f is found heterogeneous in the spanwise direction according to the emerging wavelengths λ_1 and λ_2 of the Görtler instability. We report a smooth increase of C_f from the theoretical predictions of a laminar boundary layer to those for a turbulent boundary layer over a flat plate with a slight overshoot in the domain of existence of the second dominant wavelength λ_2 .

^{a)}Electronic mail: eletta.negretti@legi.cnrs.fr

I. INTRODUCTION

Boundary layer flows are ubiquitous in both nature and engineering applications and are subject to instabilities which generally lead to the transition to turbulence. When the flow develops over a curved boundary this transition may occur through the development of the so-called Görtler instability¹⁻⁵, which results from a local unbalance between the centrifugal force and the normal pressure gradient. The boundary layer then exhibits unstable flow motion in the form of pairs of counter-rotating streamwise vortices that gives rise to longitudinal streaks, leading to strongly distorted velocity profiles and normal-to-wall flow motion correlated with local low and high momentum fluxes. Due to their direct application in industrial^{6,7} and geophysical⁸⁻¹⁰ contexts, experimental¹¹⁻¹³ and numerical¹⁴⁻¹⁶ studies on the development of the Görtler instability in boundary layer flows were performed using both wavelength-forced and wavelength-free inlet conditions. Inflow conditions showed to be a crucial choice since they lead either to a unique prescribed wavelength of the Görtler instability or to a freely developing system of multiple wavelengths.

For boundary layers developing over a flat plate, previous studies^{17,18}, highlight the importance of the inlet conditions in determining the laminar-turbulent transition, not only in terms of the transition Reynolds number $Re_{\theta,t}$ based on the momentum thickness θ and the free stream velocity U_∞ , but also influencing the formation of characteristic flow coherent structures that develop in the boundary layer. This, in turn, can strongly change the behaviour of flow properties such as the drag coefficient with important consequences in industrial and geophysical contexts. For example, Schlatter and Örlü¹⁹ showed that the skin friction coefficient C_f have very different developments depending on the tripping method used to force transition to turbulence. In general, it was observed that, for a Blasius boundary layer over a flat plate, the smaller the transition Reynolds number $Re_{\theta,t}$, the more likely an overshoot of C_f was reported departing the theoretical predictions for a turbulent boundary layer; in contrast, when $Re_{\theta,t}$ was large ($> 2,500$) a smooth increase of C_f from laminar to turbulent predictions over a flat plate has been observed (see also Méndez *et al.*²⁰).

In a Görtler flow, the typical evolution of the flow includes a first linear region characterized by a distortion of the mean flow which is well predicted by linear stability theory³, followed by a non-linear region characterized by the above-mentioned longitudinal Görtler structures with a mushroom-like spanwise section and upwash/downwash location. Swearingen and Blackwelder¹² (see also Park and Huerre²¹) concluded that the Görtler vortices do not degenerate directly to

turbulence, instead they set-up a localized shear-layer instability that results in the appearance of secondary instabilities. Their main finding was the association of the secondary instabilities with the high shears in the spanwise direction rather than with those in the wall-normal direction (see also Schultz and Volino²²).

Méndez *et al.*²⁰ studied the laminar-to-turbulent transition in a Blasius flow over a concave wall by forcing the wavelength of the Görtler instability using wall-roughness elements, following the study of Schrader, Brandt, and Zaki¹⁴, while increasing the spanwise dimension of the computational domain to assure a better transition to turbulence. They identified and characterized four regions encountered in the transition process (linear, nonlinear, transition to turbulence and fully turbulent) and performed a parametric study showing that the transition point is delayed when the radius of curvature is increased, however, at the same critical Görtler number.

So far, eighter numerical (Schrader, Brandt, and Zaki¹⁴, Méndez *et al.*²⁰ and references herein) or experimental^{8,9,11-13,22} studies focusing on the evolution of the boundary layer over a curved boundary reported the onset of only one unstable Görtler wavelength within the full considered domain. Generally, these numerical studies started with initial laminar flow conditions with the subsequent onset of one Görtler wavelength as predicted from LSA and that degenerated into a turbulent flow. The experiments also include studies where the flow already attained turbulent conditions when reaching the curved boundary. Tani¹¹ demonstrated experimentally that Görtler vortices can exist also in a turbulent boundary layer (see also Hopfinger *et al.*⁸, Albayrak, Hopfinger, and Lemmin⁹, Swearingen and Blackwelder¹²). In this cases, the dominant wavelength of the Görtler instability can be predicted using LSA, but a 'turbulent' Görtler number based on the turbulent viscosity ν_t has to be considered instead of the classical Görtler number defined using the kinematic viscosity ν .

Here, we perform well resolved Large-Eddy Simulations (LES) of a Blasius boundary layer over a concave wall. We let the Görtler instability develop freely, starting from a linear region and reaching turbulent conditions at the end of the computational domain. In particular, the Reynolds and Görtler numbers at the inlet are set to much higher values ($Re_{\theta_0} = 1,175$, $G_{\theta_0} = 75$) as compared to previous studies. In their study of boundary layer data over a flat plate, Örlü and Schlatter²³ demonstrated that starting with a high laminar $Re_{\theta} (= 750)$ yields different results not only in terms of the skin friction coefficient, but also for integral and global quantities. Here, the imposed high $G_{\theta_0} = 75$ enables reaching high enough turbulent Görtler numbers in the turbulent region to ensure the onset of a second dominant wavelength. The large spanwise domain permits

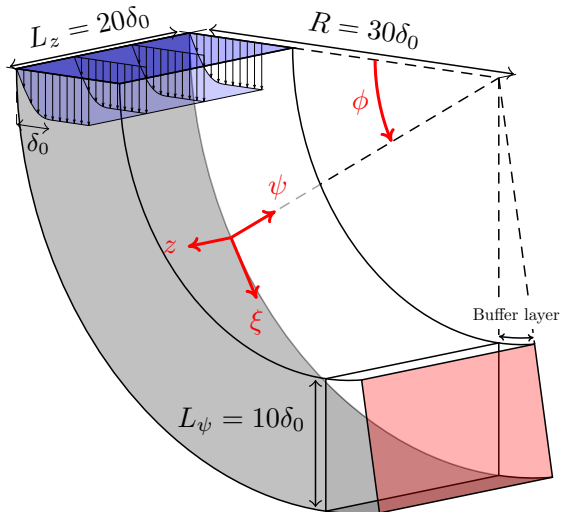


FIG. 1. Sketch of the computational domain. The inlet and outlet are highlighted in blue and red respectively. All dimensions are expressed in terms of the initial boundary layer thickness δ_0 . The domain for physical analysis spans from $\phi = 0$ to $\phi = \pi/2$, and a buffer layer is used for 10 more degrees.

the presence of up to 52 Görtler vortices in the laminar region, with the observed wavelength corresponding to the theoretical most amplified wavelength predicted by LSA for the present conditions. The skin friction coefficient is found to be accordingly heterogeneous, both in the laminar and turbulent regions with values that exceeds the predictions for a turbulent boundary layer over a flat plate in the turbulent region, similarly to Örlü and Schlatter²³.

The paper is organized as follows: in section II we describe the numerical resolution method. Section III includes results for the flow topology and the characteristic statistics of each developed region (§III A), the comparison with theoretical predictions of linear stability theory (§III B) and the effects on the skin friction coefficient (§III C). Conclusions are given in section IV.

II. NUMERICAL METHOD

Large-Eddy Simulations (LES) have been performed using the YALES2 flow solver²⁴, which solves the incompressible Navier-Stokes equations for turbulent flows on unstructured meshes using a projection method for pressure-velocity coupling²⁵. It relies on fourth-order central finite-volume schemes and on highly efficient linear solvers²⁶. The time integration is explicit for convective terms using a fourth-order modified Runge-Kutta scheme, with a semi-implicit integration for the diffusive terms. We used unstructured grids composed by prisms and tetrahedron elements,

	Re_{θ_0}	G_{θ_0}	$\left(\frac{R}{\theta_0}\right)^{1/2}$	Transition method	$\Delta\xi^+ \times \Delta\psi^+ \times \Delta z^+$
Méndez <i>et al.</i> ²⁰	75	1.5	50.0	Roughness elements	$19.10 \times 0.55 \times 5.80$
Schrader, Brandt, and Zaki ¹⁴	75	1.5	50.0	Roughness elements	$15.70 \times 0.70 \times 7.10$
Schultz and Volino ²²	133	5.3	25.0	Free-stream turbulence	-
Present study	210	13.4	16.0	Numerical noise	$4.90 \times 0.17 \times 4.90$
Present study	290	18.4	16.0	Numerical noise	$4.90 \times 0.17 \times 4.90$
Present study	1175	75.0	16.0	Numerical noise	$4.90 \times 0.17 \times 4.90$
Örlü and Schlatter ²³	55	∞	0.0	Tripping at $Re_{\theta} = 55$	$25.30 \times 14.2 \times 10.8$
Örlü and Schlatter ²³	750	∞	0.0	Tripping at $Re_{\theta} = 750$	$25.30 \times 14.2 \times 10.8$

 TABLE I. Physical configuration and numerical resolution. References are sorted by G_{θ_0} in ascending order.

allowing to have a high resolution of the near-wall region. The dynamic Smagorinsky subgrid-scale model is used²⁷.

A sketch of the computational domain is given in figure 1. A local frame (ξ, ψ, z) is used to conveniently characterize the flow in the present curved domain, where ξ , ψ and z are the stream-wise, wall-normal and spanwise directions, respectively. The inlet velocity is set to a Blasius boundary layer with a thickness δ_0 and a free-stream velocity U_{∞} . The geometry of the computational domain is a 90-degree concave channel with constant curvature $R = 30\delta_0$, with a spanwise length $L_z = 20\delta_0$ and a wall-normal length $L_{\psi} = 10\delta_0$. Close to the wall, the mesh size in the streamwise, wall-normal and spanwise directions is $\Delta\xi = 3.6 \times 10^{-2}\delta_0$, $\Delta\psi = 1.2 \times 10^{-3}\delta_0$ and $\Delta z = 3.6 \times 10^{-2}\delta_0$ respectively, for a total number of mesh cells $N_c = 2.4 \times 10^8$. This ensures that the mesh size at the wall, expressed in wall unit $^+$ (normalization with the wall friction velocity u_{τ} , and the kinematic viscosity ν), are $(\Delta\xi^+, \Delta\psi^+, \Delta z^+) = (4.90, 0.17, 4.90)$ at the inlet and reach maximum values of $(\Delta\xi^+, \Delta\psi^+, \Delta z^+) = (28.20, 0.98, 28.20)$ in the turbulent region. At the bottom and top boundaries (outer and inner radii boundaries), no-slip and free-slip boundary conditions are prescribed, respectively. The flow is set to be periodic in the spanwise direction. At the end of the 90-degree domain, a buffer layer is used ($90^\circ < \phi < 100^\circ$) and a convective outflow²⁸ after ($\phi = 100^\circ$).

We let Görtler vortices develop spontaneously without forcing the spanwise wavelength, with-

Linear to turbulent Görtler instability transition

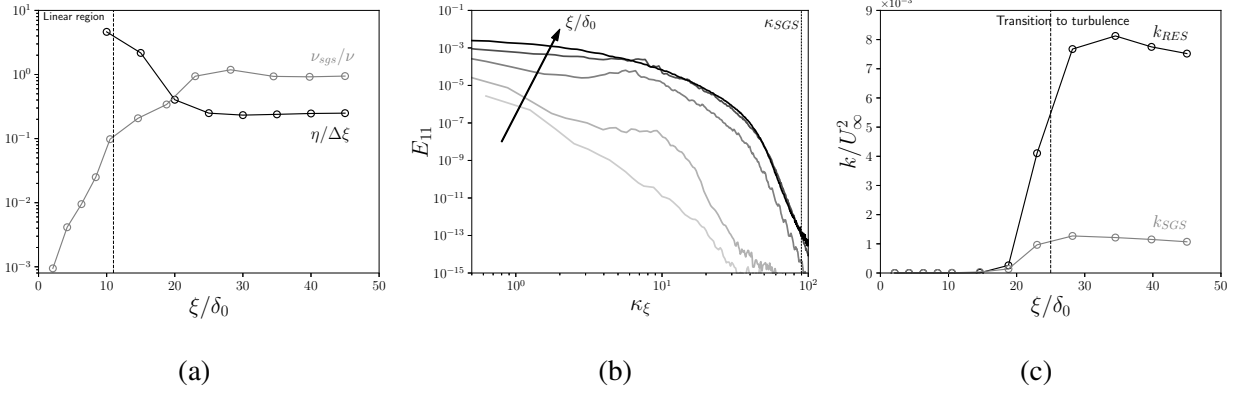


FIG. 2. (a) Ratio between the Kolmogorov scale η and the mesh size in the streamwise direction $\Delta\xi$ (black line), along with the ratio between the sub-grid viscosity ν_{SGS} and the kinematic viscosity of the fluid ν . (b) Streamwise evolution of the energy spectrum E_{11} for $\xi/\delta_0 = 10, 15, 20, 25, 35$ (from light grey to black). (c) Streamwise evolution of the explicitly resolved TKE k_{RES} and the sub-grid TKE k_{SGS} .

out free-stream turbulence level nor white noise perturbations. Hence, the centrifugal instability is triggered by numerical noise. The spanwise length of the computational domain was chosen in order to get up to 52 Görtler rolls within the initial linear region, based on linear stability predictions where the expected non-dimensional wavelength is $\Lambda = (U_\infty \lambda / \nu) (\lambda / R)^{1/2} = 500$, where λ is the wavelength defined as the distance between two pairs of counter-rotating Görtler vortices. This allows to reach converged spatial statistics in the spanwise direction in both the linear and turbulent regions. The Reynolds number based on the inflow boundary layer thickness δ_0 is $Re_{\delta_0} = (U_\infty \delta_0) / \nu = 10,000$ while the Reynolds number based on the inflow momentum thickness is $Re_{\theta_0} = (U_\infty \theta_0) / \nu = 1,175$. The Görtler number is consequently $G_{\theta_0} = Re_{\theta_0} (\theta_0 / R)^{1/2} = 75$.

A. Numerical validation and turbulent state

Figure 2a displays the streamwise evolution of the Kolmogorov scale $\eta = (\nu^3/\varepsilon)^{1/4}$ (explicitly determined using structure functions²⁹) normalized by the longitudinal mesh size $\Delta\xi$ (black line) and the evolution of the sub-grid eddy viscosity ν_{SGS} normalized by the kinematic viscosity ν (grey line). We see that $\nu_{SGS}/\nu \ll 1$ and $\eta/\Delta\xi \approx 5$ in the linear region, so that the chosen grid size at the wall in the linear region ($\xi/\delta_0 \leq 11$) is sufficiently small to resolve all scales and the LES is practically equivalent to a DNS.

Figure 2b gives the energy spectrum as a function of the streamwise wavenumber $\kappa\xi$ at different streamwise positions (different solid lines), showing that starting from $\xi/\delta_0 = 10$ all energetic

Linear to turbulent Görtler instability transition

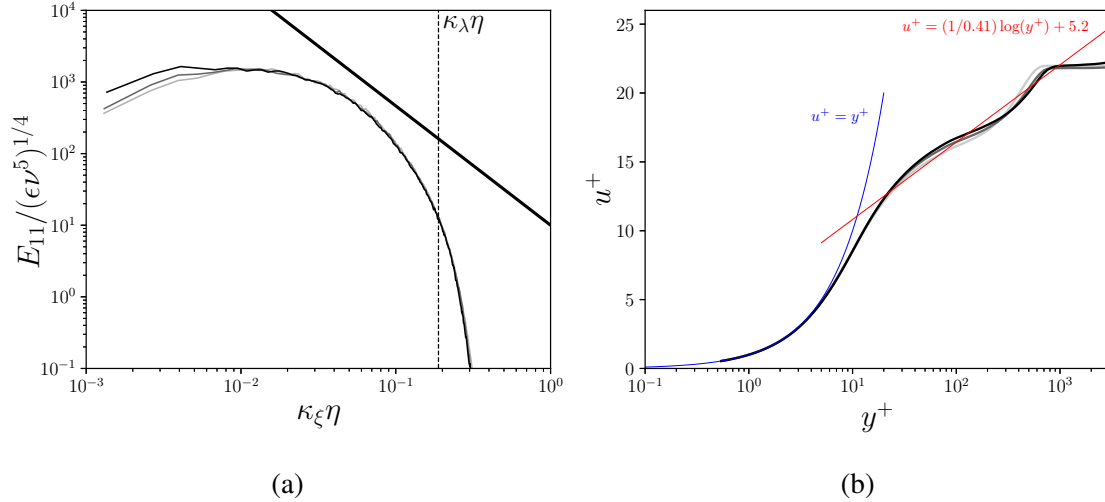


FIG. 3. (a) Normalized energy spectrum for $\xi/\delta_0 = 35, 40, 45$ (from light grey to black solid lines), with the $-5/3$ slope (black solid line) and the Taylor micro-scale (vertical dotted line). (b) Velocity profiles in wall units $u^+ = f(y^+)$ for $\xi/\delta_0 = 35, 40, 45$ (from light grey to black circles).

scales are resolved. Further downstream, we see the evolution of the spectra consistent with an energy transfer from small to larger wavenumbers up to the cut-off wavenumber κ_{SGS} (see vertical dotted line in figure 2b) representative of the sub-grid model. Figure 2c shows the streamwise evolution of the normalized directly resolved (k_{RES}) and modeled (k_{SGS}) turbulent kinetic energy (TKE). After transition to turbulence, k_{RES} accounts for less than 20% of the total TKE, which gives a criterion for good LES resolution^{29,30}.

To assess the turbulence level reached in the last part of the computational domain we plot in figure 3a the normalized energy spectrum $E_{11}/(\epsilon \nu^5)^{1/4}$ as a function of κ_ξ/η for $\xi/\delta_0 = (35, 40, 45)$. The spectra converge and the inertial zone (i.e. Taylor microscale $\kappa_\lambda \eta$, dashed black line) is partially resolved and consistent with a $-5/3$ power law. We also estimated the Reynolds number $Re_\lambda = u'\lambda/\nu$ based on the Taylor microscale $\lambda = (\nu u'^2/\epsilon)^{1/2}$ and found values $Re_\lambda > 100$ for $\xi/\delta_0 > 15$, with an increasing value up to $Re_\lambda \approx 200$ at the end of the computational domain.

The velocity profiles expressed in wall-units $u^+ = f(y^+)$ computed at the end of the domain ($\xi/\delta_0 = (35, 40, 45)$) are displayed in figure 3b. They converge toward a turbulent velocity profile in agreement with the log-law $u^+ = (1/0.41) \log(y^+) + 5.2$ found in turbulent boundary layers over flat plates. We note that the velocity profiles exhibit an inflection point, specific of a secondary motion in the flow induced by the presence of Görtler vortices.

An overall assessment of the boundary layer development can be obtained through the boundary

Linear to turbulent Görtler instability transition

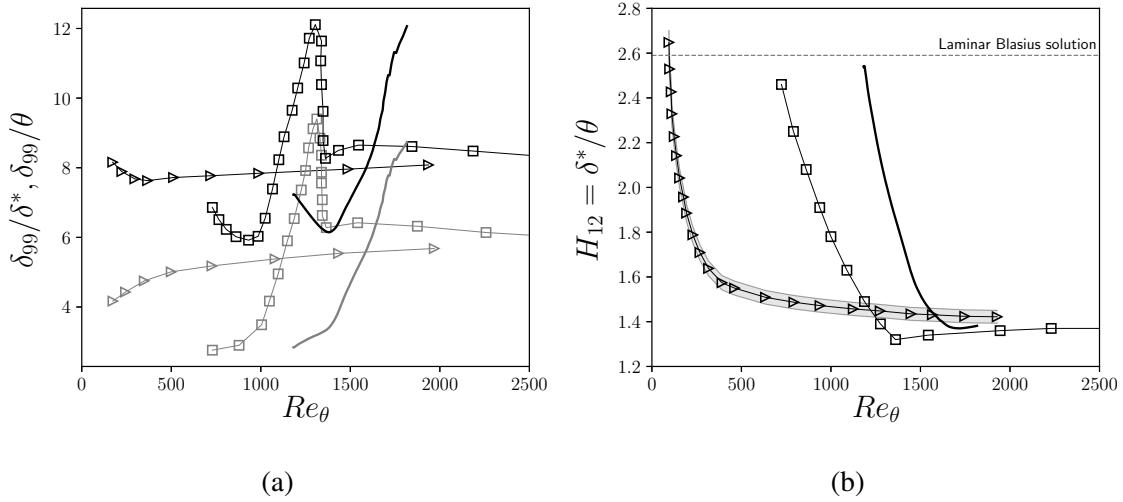


FIG. 4. (a) Evolution of the boundary layer thickness δ_{99} normalized by the displacement thickness δ^* (grey) and the momentum thickness θ (black) versus Re_θ . Present results with $Re_{\theta_0} = 1175$ (solid lines) are compared with results from Örlü and Schlatter²³ (squares: $Re_{\theta_0} = 750$; triangles: $Re_{\theta_0} = 55$). (b) Shape factor as a function of Re_θ . A 2% error with respect to results from Örlü and Schlatter²³ at $Re_{\theta_0} = 55$ is highlighted in grey.

layer thickness δ_{99} as well as its integral measures, i.e. the displacement (δ^*) and momentum-loss (θ) thicknesses. The ratio between δ_{99} and δ^* (grey solid line) and θ (black solid line) is depicted in figure 4a, along with the the shape factor ($H_{12} = \delta^*/\theta$) in 4b, as a function of Re_θ . We compare our results to those of Örlü and Schlatter²³ for two cases: the first having $Re_{\theta_0} = 55$ (triangles) and the second with $Re_{\theta_0} = 750$ (squares). As pointed out by Örlü and Schlatter²³, a strong increase of the normalized boundary layer thicknesses occurs when transitioning to turbulence if the initial Reynolds number is large ($Re_{\theta_0} = 750$ for Örlü and Schlatter²³ and $Re_{\theta_0} = 1,175$ in the present study), which clearly contrasts with the smooth increase in the case of $Re_{\theta_0} = 55$. The shape factor H_{12} reveals a similar behaviour as in the case of Örlü and Schlatter²³ with a turbulent state reached at the end of the computational domain however with values that are 8% of the convergence limit (cf. Örlü and Schlatter²³). These results confirm thus the findings of Örlü and Schlatter²³ for which starting with a higher laminar $Re_{\theta,0}$ retards reaching the fully turbulent regime.

Linear to turbulent Görtler instability transition

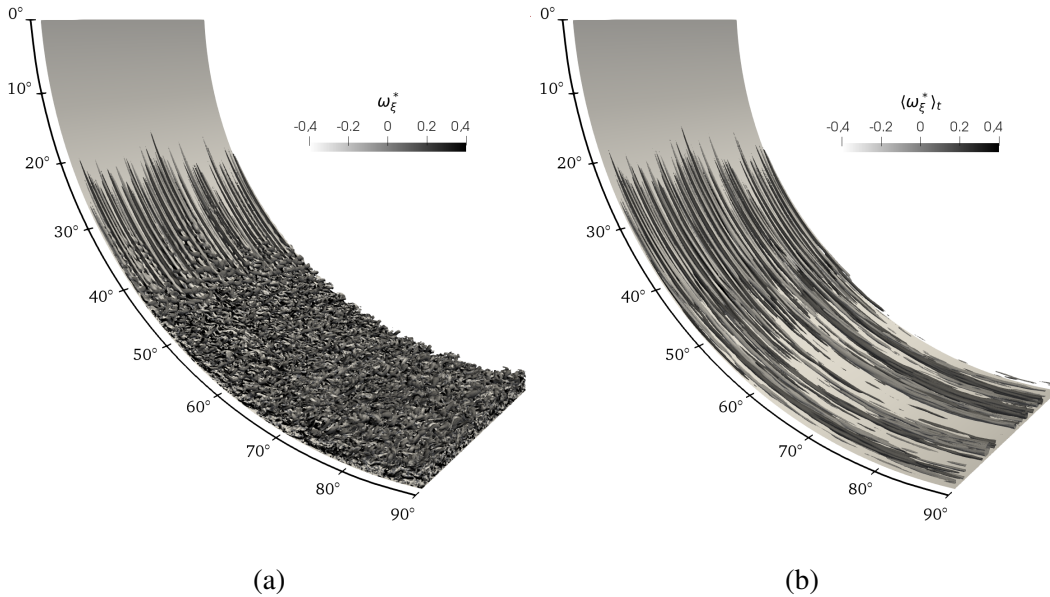


FIG. 5. Three-dimensional views of iso-contours of the normalized Q -criterion $Q^* = QR^2/U_\infty^2 = 1$, computed from the instantaneous flow velocity field (a) and the mean flow velocity field (b) colored by the instantaneous non-dimensional vorticity $\omega_\xi^* = \omega_\xi \delta_0/U_\infty$ and the mean non-dimensional streamwise vorticity $\langle \omega_\xi^* \rangle_t = \langle \omega_\xi \rangle_t \delta_0/U_\infty$. Streamwise streak structures (Görtler vortices) are visible in the non-linear region of the instability ($22^\circ < \phi < 42^\circ$), and persistent in the turbulent region (b).

III. RESULTS

In the following, ensemble average $\langle \cdot \rangle$ is performed along homogeneous samples. Averaging over time at each point (ξ, ψ, z) provides e.g. temporal mean velocity $\langle \mathbf{u} \rangle_t(\xi, \psi, z)$, where $\mathbf{u} = (u, v, w)$ is the vector of the three velocity components in the longitudinal, wall-normal and spanwise directions respectively. Additional averaging along the spanwise direction of the domain provides temporal and spatial mean velocities, e.g. $\langle \mathbf{u} \rangle_{t,z}(\xi, \psi)$.

A. Flow topology

The topology of the flow is described using a non-dimensional Q -criterion defined as $Q^* = (\Omega_{ij}\Omega_{ij} - S_{ij}S_{ij}) / (2\delta_0^2/U_\infty^2)$. Herein, Ω_{ij} is the vorticity tensor and S_{ij} the strain rate tensor. A three-dimensional view of the iso-contours of the Q -criterion set to $Q^* = 10^{-3}$ is shown in figure 5. Figure 5(a) is computed from the instantaneous velocity field \mathbf{u} colored by the instantaneous non-dimensional streamwise vorticity $\omega_\xi^* = \omega_\xi \delta_0/U_\infty$, while figure 5(b) is computed from the

Linear to turbulent Görtler instability transition

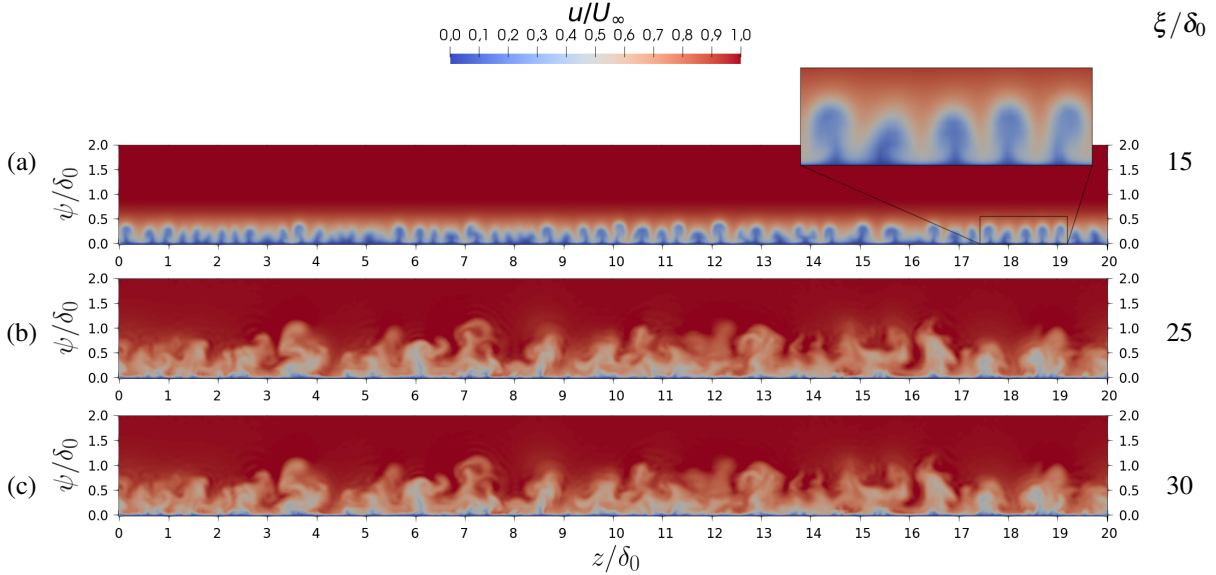


FIG. 6. Instantaneous streamwise velocity field u/U_∞ at $\xi/\delta_0 = 15$ (a), 25 (b) and 30 (c). In (a) mushroom-like structures of the Görtler instability are evident (see inset for a zoomed view). For $\xi/\delta_0 > 25$ (b-c), a scale multiplicity is observed in the instantaneous velocity fields (i.e. turbulent state).

mean flow $\langle \mathbf{u} \rangle_t$ colored by the mean non-dimensional streamwise vorticity $\langle \omega_\xi^* \rangle_t = \langle \omega_\xi \rangle_t \delta_0 / U_\infty$. The longitudinal streak structures present for $21^\circ < \phi < 42^\circ$ are observed both in figures 5(a) and 5(b) meaning that they are spatially steady, which is characteristic for Görtler vortices. In figure 5(a), we see that the onset of the Görtler vortices appears at about $\xi/\delta_0 = 11$ ($\phi = 21^\circ$, $Re_\theta = 1,200$), and the transition to turbulence starts at about $\xi/\delta_0 = 22$ ($\phi = 42^\circ$, $Re_\theta = 1350$). The turbulent region is reached at $\xi/\delta_0 > 31$ ($\phi > 59^\circ$, $Re_\theta = 1,500$) (see also §II A). The iso-contour of the Q -criterion computed from the mean flow velocity field (figure 5b) exhibits large scale longitudinal vortical Görtler structures in both the transition and in the turbulent region. Spanwise instantaneous streamwise velocity fields are displayed in figure 6 at three different streamwise locations $\xi/\delta_0 = (15, 25, 30)$ (a,b,c, respectively) highlighting the typical mushroom like structure of the Görtler instability¹³, well defined in the initial development region (figure 6a) while figure 6(b,c) shows the onset of scale multiplicity further downstream.

Since the Görtler vortices are spatially steady, they induce a distortion of the mean flow⁵ which leads to a spanwise heterogeneity of the flow properties. A measure of the spanwise heterogeneity level (SHL) of the mean flow has been proposed by Méndez *et al.*²⁰ as follows:

$$\mathbf{u}_{SHL}(\xi) = \sqrt{\frac{1}{L_z} \int_0^{L_z} [\langle \mathbf{u} \rangle_t'(\xi, \psi, z)]^2 dz}, \quad (1)$$

Linear to turbulent Görtler instability transition

where $\langle \mathbf{u} \rangle'_t(\xi, \psi, z) = \langle \mathbf{u} \rangle_t(\xi, \psi, z) - \langle \mathbf{u} \rangle_{t,z}(\xi, \psi)$ is the spanwise fluctuation of the mean velocity field $\langle \mathbf{u} \rangle_t(\xi, \psi, z)$.

Equation (1) represents the spanwise standard deviation of the temporal mean flow, and the streamwise evolution of its value at the wall-normal position $\psi = 0.25\delta_0$ is displayed in figure 7(a). We see that all three components of \mathbf{u}_{SHL} rapidly increase in the first region which corresponds to the linear growth of the Görtler instability and starts to saturate at $\xi/\delta_0 \approx 11$. The level of heterogeneity is maintained for $\xi/\delta_0 > 25$ for all three components. This is not observed in a turbulent boundary layer over a flat plate, where a statistical spanwise homogeneity of the flow is expected.

Selected profiles of \mathbf{u}_{SHL} are shown in figure 7(b) along with the associated mean streamwise velocity profiles $\langle u \rangle_{t,z}$. At $\xi/\delta_0 = 10$ (linear region), the computed $\langle u \rangle_{t,z}$ matches the Blasius solution. u_{SHL} and v_{SHL} have maximum values for $\psi/\delta_0 = 0.12$ and $\psi/\delta_0 = 0.16$, respectively while w_{SHL} has two maxima reached for $\psi/\delta_0 = 0.05$ and $\psi/\delta_0 = 0.28$. Note that the wall-normal positions of the maxima of all three components of \mathbf{u}_{SHL} are consistent with the observation of the Görtler vortices (cf. figure 6a). At $\xi/\delta_0 = 25$ (non-linear region), an inflection point is observed on the mean streamwise velocity profile $\langle u \rangle_{t,z}$ (grey line in figure 7b), which is due to the development of the Görtler vortices. Wall-normal profiles of u_{SHL} and w_{SHL} are strongly influenced by the non-linear effects and the wavelength multiplicity thus having complex shapes while the v_{SHL} profile shape remains nearly the same. The width of all three profiles is thickening in the non-linear region, which might be associated with a sudden increase of turbulent state (see the appearance of three-dimensional structures in figure 5a and non-linear saturation in figure 7a). At $\xi/\delta_0 = 40$ in the turbulent region, the mean velocity profile as well as \mathbf{u}_{SHL} profiles are thicker, and an inflection point is still observed on the $\langle u \rangle_{t,z}$ profile, consistent with the large-scale streamwise vortices observed in the turbulent region (figure 5c). In this region, u_{SHL} and w_{SHL} have their maximum value very close to the wall at $\psi/\delta_0 = 0.08$, while v_{SHL} still keeps the same profile shape and its maximum moves away from the wall, similarly to what is observed when Görtler vortices grow in the non-linear region.

In order to extract the wavelengths responsible for the spatial heterogeneity, we focus on the wall-normal component of the velocity, which is associated with the upwash and downwash motions, characteristic of the Görtler instability. A spatial FFT is therefore performed in the spanwise direction on the velocity fluctuation $\langle v \rangle'_t$ and the streamwise evolution of the power spectral density is shown in figure 8(a). Unlike the previous studies of Méndez *et al.*²⁰ and Schrader, Brandt, and

Linear to turbulent Görtler instability transition

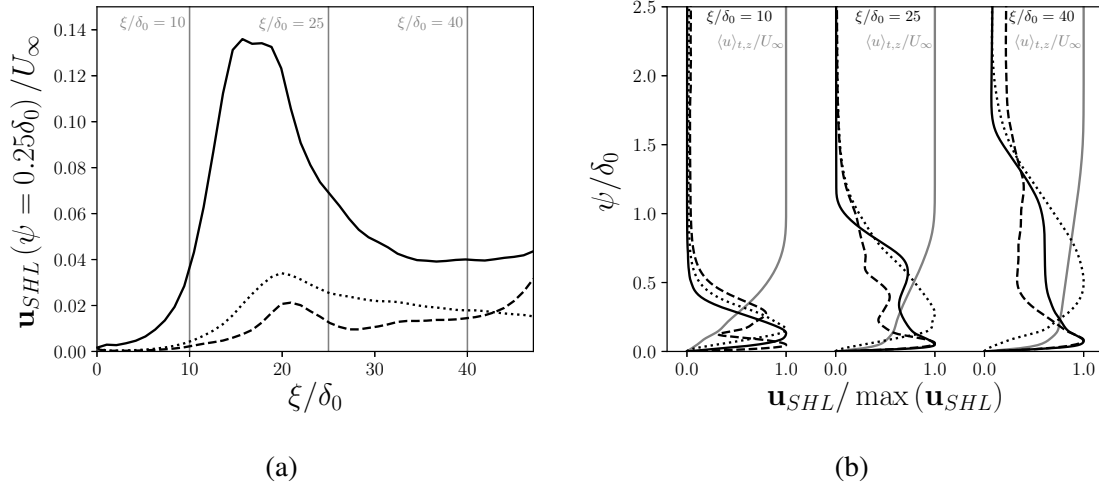


FIG. 7. (a) Streamwise evolution of \mathbf{u}_{SHL} at $\psi = 0.25\delta_0$ (Eq. 1) for the longitudinal (solid line), wall-normal (dashed line), and spanwise (dotted line) velocity components with the saturation reached at $\xi/\delta_0 \approx 22$. (b) Selected vertical profiles at $\xi/\delta_0 = (10, 25, 40)$ (from left to right, respectively) for \mathbf{u}_{SHL} and normalized by their maximum. The grey solid lines in (b) represent the base state Blasius profile.

Zaki¹⁴ where the instability wavelength is forced, here we report the onset of various wavelengths, also observed in Tandiono, Winoto, and Shah¹³.

In the linear region ($2 < \xi/\delta_0 < 11$), multiple wavelengths can be identified (cf. figure 8a), and the most amplified wavelength is found to be $\lambda_1 = 0.385\delta_0$. λ_1 is dominant for $2 < \xi/\delta_0 < 22$ which corresponds to both linear and non-linear regions. At the breakdown of the Görtler vortices (figure 7a), larger wavelengths ($0.5\delta_0 < \lambda < 1.0\delta_0$) are found in the spectrum which persist only for a distance $\Delta\xi \approx 6\delta_0$.

Further downstream in the turbulent region ($\xi/\delta_0 > 30$), the dominant wavelength in the flow is found to be $\lambda_2 = 1.55\delta_0$.

B. Comparison to linear stability theory

In order to estimate the theoretical predicted growth rates and most unstable wavelengths, we extended the LSA of Floryan and Saric³ for a larger domain of the non-dimensional wavenumber $0.03 < \alpha\theta < 3.0$, with $\alpha\theta = (2\pi/\lambda)\theta$, and for Görtler numbers $0.5 < G_\theta < 100.0$. For this, we considered the linear perturbation equations of continuity and momentum for a Blasius boundary layer over a curved wall using a normal modes approach. The governing stability equations read

Linear to turbulent Görtler instability transition

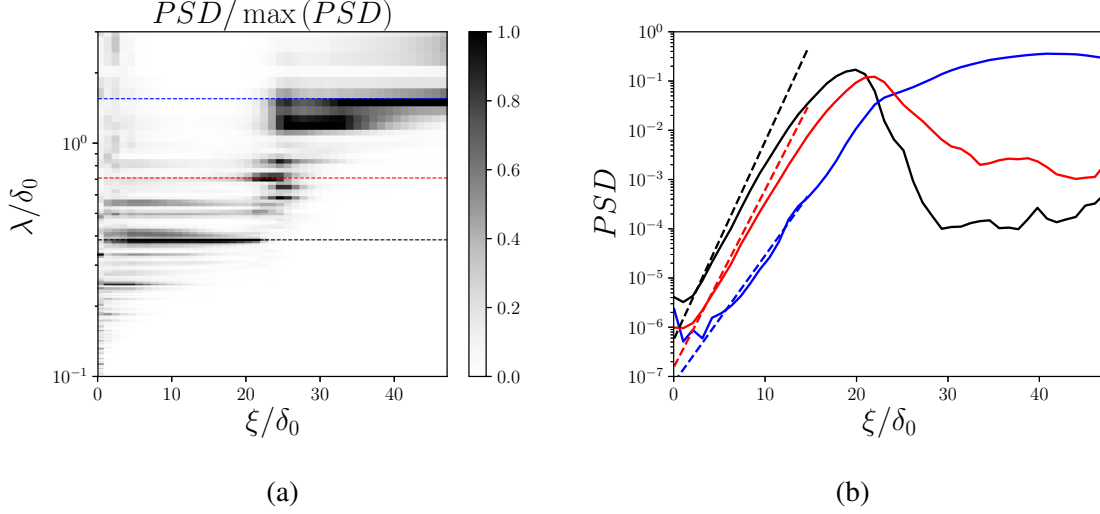


FIG. 8. (a) Spectrogram from a spatial FFT in the spanwise direction on the wall-normal disturbance velocity $\langle v \rangle_t'$ normalized by the local maximum amplitude. Two dominant wavelengths emerge in the different development regions: $\lambda_1 = 0.385\delta_0$ (linear region, black dotted line), $\lambda_2 = 1.55\delta_0$ (turbulent region, blue dotted line) and an intermediate wavelength $\lambda = 0.709\delta_0$ (red dotted line); (b) respective streamwise evolution of the power spectral densities (solid lines) with the theoretical growth from LSA (dashed lines).

then

$$\beta \hat{u} + \frac{d\hat{v}}{d\psi} + \alpha \hat{w} = 0 \quad (2)$$

$$\hat{u} \frac{\partial U}{\partial \xi} + \beta U \hat{u} + \hat{v} \frac{\partial U}{\partial \psi} + V \frac{d\hat{u}}{d\psi} - \frac{d^2 \hat{u}}{d\psi^2} + \alpha^2 \hat{u} = 0 \quad (3)$$

$$\beta U \hat{v} + \hat{u} \frac{\partial V}{\partial \xi} + \hat{v} \frac{\partial V}{\partial \psi} + V \frac{d\hat{v}}{d\psi} + 2G^2 U \hat{u} + \frac{d\hat{p}}{d\psi} - \frac{d^2 \hat{v}}{d\psi^2} + \alpha^2 \hat{v} = 0 \quad (4)$$

$$\beta U \hat{w} + V \frac{d\hat{w}}{d\psi} - \alpha \hat{p} - \frac{d^2 \hat{w}}{d\psi^2} + \alpha^2 \hat{w} = 0 \quad (5)$$

where the perturbation velocities are defined as

$$[u', v', p'] = [\hat{u}(\psi), \hat{v}(\psi), \hat{p}(\psi)] \cos(\alpha z) \exp(\beta \xi) \quad (6)$$

$$w' = \hat{w}(\psi) \sin(\alpha z) \exp(\beta \xi) \quad (7)$$

with (U, V) the base flow, α the wavenumber, β the spatial growth rate and $(\hat{u}, \hat{v}, \hat{w})$ the spatial modes.

The system of equations (2–5) is expressed in matrix form through M_{ij}

$$\frac{d\zeta_i}{d\psi} = M_{ij}(\psi) \zeta_j \quad (8)$$

Linear to turbulent Görtler instability transition

where $\zeta_1 = \hat{u}$, $\zeta_2 = \frac{d\hat{u}}{d\psi}$, $\zeta_3 = \hat{v}$, $\zeta_4 = \frac{d\hat{v}}{d\psi}$, $\zeta_5 = \frac{d^2\hat{v}}{d\psi^2}$, $\zeta_6 = \frac{d^3\hat{v}}{d\psi^3}$, which constitutes an eigenvalue problem with boundary conditions

$$\zeta_1 = \zeta_3 = \zeta_4 = 0 \text{ for } \psi = 0 \quad (9)$$

$$\zeta_1 = \zeta_3 = \zeta_4 = 0 \text{ for } \psi \rightarrow \infty, \quad (10)$$

for which solutions exist only for specific sets of $(\alpha, \beta, G)^3$. It is solved as a boundary value problem using a 4th-order Runge-Kutta integration method following the work of Petitjeans³¹. The value of β which fulfills the boundary conditions (10) is calculated for a set of given (G, α) values^{3,31}.

Figure 8(b) is extracted from figure 8(a) for the two dominant wavelengths λ_1 (black line) and λ_2 (blue line) along with an intermediate wavelength of about $2\lambda_1$ (red line). It shows the stream-wise evolution of the energy contained in the wall-normal component of the velocity fluctuations for each of the above identified wavelengths. The estimated theoretical growth rates for each of these three wavelengths are reported in figure 8(b) as linear dashed lines, revealing a good agreement between the LSA predictions and the simulation results. The energy associated with λ_1 and $2\lambda_1$ is damped further downstream at $\xi/\delta_0 \approx 25$, while the energy associated with λ_2 keeps growing, hence becoming the dominant wavelength for $\xi/\delta_0 \geq 30$ until the end of the computational domain.

We predict the theoretical most amplified wavelength for the Görtler number $G_{\theta_0} = 75$ and a base flow corresponding to a Blasius boundary layer in the linear region of $\lambda_1^{th} = 0.38\delta_0$, which matches the present observation.

As already observed experimentally^{8,9,11,12} the Görtler instability may exist also in a fully developed turbulent boundary layer. Tani¹¹ argued that the *laminar* boundary layer Görtler instability diagram can be used to determine the instability characteristics of a *turbulent* boundary layer if the kinematic viscosity is replaced by the turbulent viscosity in the definition of the Görtler number. In this case, a turbulent Görtler number is the relevant parameter, defined as $G_T = U_\infty \theta / \nu_t (\theta/R)^{1/2}$. Figure 9(a) (solid line) displays the turbulent Görtler number G_T , in which the turbulent viscosity is estimated using the same approach of Tani¹¹, who assumed a constant turbulent viscosity in the outer part of the boundary layer, for which Clauser³² suggested the expression $\nu_t = 0.018U_\infty \delta^*$, where δ^* is the displacement thickness. We also estimated the G_T by calculating directly the turbulent viscosity using the Boussinesq hypothesis as

Linear to turbulent Görtler instability transition

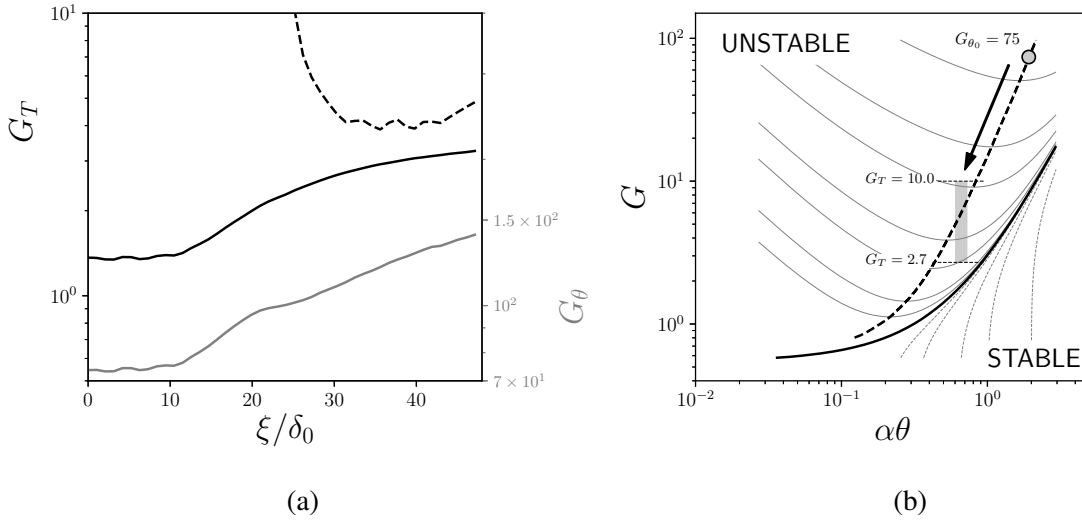


FIG. 9. (a) Variation of the turbulent Görtler number G_T in the longitudinal direction calculated using the turbulent viscosity with the mixing length model $\nu_t = 0.018U_\infty\delta^*$ from Clauser³² (solid line), where δ^* is the displacement thickness, and from the Boussinesq hypothesis $\nu_t = -\langle u'v' \rangle_{t,z}/\partial_\psi \langle u \rangle_{t,z}$ (dashed line). For comparison, G_θ is also plotted (grey line). (b) Curves of constant non-dimensional amplification rates $\beta\theta Re_\theta$. The black thick solid line and thick dashed lines correspond to the stability limit and the curve of maximum amplification rate, respectively. Present LES results are highlighted by the grey box, considering the turbulent Görtler number $G_T = U_\infty\theta/\nu_t(\theta/R)^{1/2}$.

$\nu_t = -\langle u'v' \rangle_{t,z}/\partial_\psi \langle u \rangle_{t,z}$ (dashed line). Figure 9 includes also the classical Görtler number G_θ based on the kinematic viscosity ν (grey line) for comparison. We see that both estimations for G_T are very similar, and the turbulent Görtler number ranges within $2.7 < G_T < 10$ in the turbulent region for $\xi > 25\delta_0$.

The spatial amplification rate curves obtained from the LSA are displayed in figure 9(b), with the thick black line being the neutral stability curve. The range of the reported turbulent Görtler numbers G_T and normalized wavenumbers $\alpha\theta$ (note that $\alpha\theta$ varies with θ since the wavelength λ_2 is kept constant) extracted from the present LES are highlighted within the grey box: the turbulent domain is clearly Görtler unstable. Moreover, the dominant wavelength observed in the present simulation, λ_2 , corresponds to a normalized wavenumber $\alpha\theta \approx 0.6$ that fairly fits the dominant wavenumber given by the LSA, represented by the dashed line of maximum amplification rate in figure 9(b). Hence, during transition to turbulence, the effective Görtler number decreases (from $G_{\theta,0}$ to G_T), favoring the onset of larger wavelengths, in accordance with the theoretical LSA predictions and with the present observations. In previous numerical studies $G_{\theta,0}$ is smaller (cf.

table I) so that the turbulent Görtler number falls close or even below the neutral stability curve (cf. figure 9b). Also, at such smaller G_T the most unstable modes have smaller wavenumbers so that the formation of Görtler vortices may be inhibited by a limited computational domain in the spanwise direction.

From the spectral analysis, we find that in the linear region, the equivalent number of pairs of counter-rotating vortices corresponding to the most amplified wavelength λ_1 is $N_{\lambda_1} = 52$, which is sufficiently large to perform a phase-based statistical study in the spanwise direction with converged statistics. Considering that the spanwise flow heterogeneity is mainly driven by the dominant wavelength, the phase-averaged velocity field $\langle \tilde{\mathbf{u}} \rangle_t(\xi, \psi, \bar{z})$ is defined as:

$$\langle \tilde{\mathbf{u}} \rangle_t(\xi, \psi, \bar{z}) = \frac{1}{N_{\lambda_\kappa}} \sum_{i=0}^{N_{\lambda_\kappa}-1} \langle \mathbf{u} \rangle_t(\xi, \psi, \bar{z} + i\lambda_\kappa), \quad (11)$$

where $\bar{z} \in [0, \lambda_\kappa]$ is the reduced spanwise component, and $\kappa = 1, 2$ represents the two dominant wavelengths. Similarly, we introduce the phase-averaged fluctuation velocity field $\langle \tilde{\mathbf{u}} \rangle'_t(\xi, \psi, \bar{z}) = \langle \tilde{\mathbf{u}} \rangle_t(\xi, \psi, \bar{z}) - \langle \mathbf{u} \rangle_{t,z}(\xi, \psi)$.

In the linear region, the computed velocity field within \bar{z} is compared with the theoretical expression of the spatial modes $\hat{\mathbf{u}}$. We expect the present results to fit the expression of the velocity disturbances defined in the LSA:

$$\langle \tilde{\mathbf{u}} \rangle'_t(\xi, \psi, \bar{z}) = \hat{\mathbf{u}}(\psi) [\cos(\alpha\bar{z}), \cos(\alpha\bar{z}), \sin(\alpha\bar{z})] \exp(\beta\xi). \quad (12)$$

In order to compute the spatial mode $\hat{\mathbf{u}}$ using equation (12), we perform a cross-correlation of the fluctuation velocity $\langle \tilde{\mathbf{u}} \rangle'_t$ and the harmonic functions $[\cos(\alpha\bar{z}), \cos(\alpha\bar{z}), \sin(\alpha\bar{z})]$, where α is obtained using the spanwise FFT. The spatial growthrate β is not needed since $\hat{\mathbf{u}}$ is normalized by the maximum value of \hat{u} denoted \hat{u}_{max} ³.

The ensemble average profiles at $\xi/\delta_0 = 7$ representative of the linear region are shown in figure 10 (a-c) as solid lines and compared with the obtained LSA solutions (dashed lines). The dispersion of the computed local modes are highlighted with the shaded regions. The agreement is good, with exception of a slight shift between the two curves and an overestimation of \hat{v} , more likely due to the simultaneous presence of other wavelengths with similar amplitudes in the simulation profiles, as observed in figure 8(a).

The same statistical analysis is applied to the higher dominant wavelength λ_2 , both in the initial linear region ($2 < \xi < 11\delta_0$) and in the turbulent region ($\xi > 35\delta_0$) (figure 10 (d-f)). In the linear region, spatial modes associated with λ_2 obtained from the simulation compare well with the

Linear to turbulent Görtler instability transition

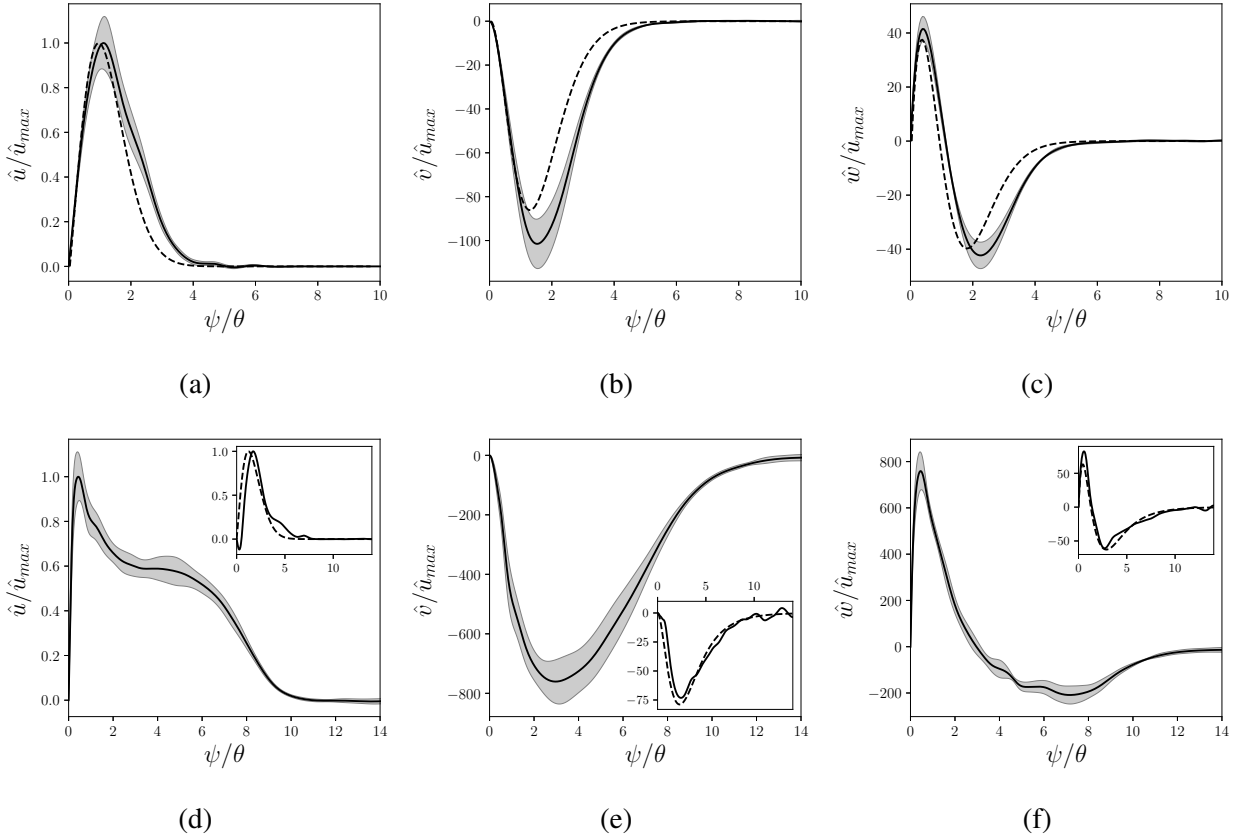


FIG. 10. Ensemble average of the spatial modes ($\hat{u}, \hat{v}, \hat{w}$) normalized by \hat{u}_{max} obtained from LES (solid lines) and theoretical predictions using LSA (dashed lines). Dispersion of the local modes from the LES simulation is highlighted by the shaded grey regions. (a-c) Spatial modes associated with λ_1 in the linear region ($\xi/\delta_0 = 7$). (d-f) Spatial modes associated with λ_2 in the turbulent region ($\xi/\delta_0 = 40$), with insets showing the spatial modes associated with λ_2 in the linear region, compared to LSA.

LSA modes (insets of figure 11, bottom panels), meaning that λ_2 is present and grows from the beginning of the computational domain. It is found that the local disturbance velocity modes collapse, and a unique spatial mode emerges. In the turbulent region, the spatial modes have a similar shape as those in the linear region but with a relaxation of the profile in the normal direction; more importantly \hat{u} is strictly positive, \hat{v} is strictly negative and \hat{w} is positive near the wall and negative in the outer layer, as it is the case in the initial linear growth region. In terms of amplitude, the observed spatial modes associated with λ_2 have a much larger amplitude in the turbulent region than in the linear region, as expected. The existence of the spatial modes in the turbulent region is thus consistent with the observation of streamwise Görtler-like vortices in the turbulent region reported in figure 5(b). This shows that spatial modes for the disturbance velocity

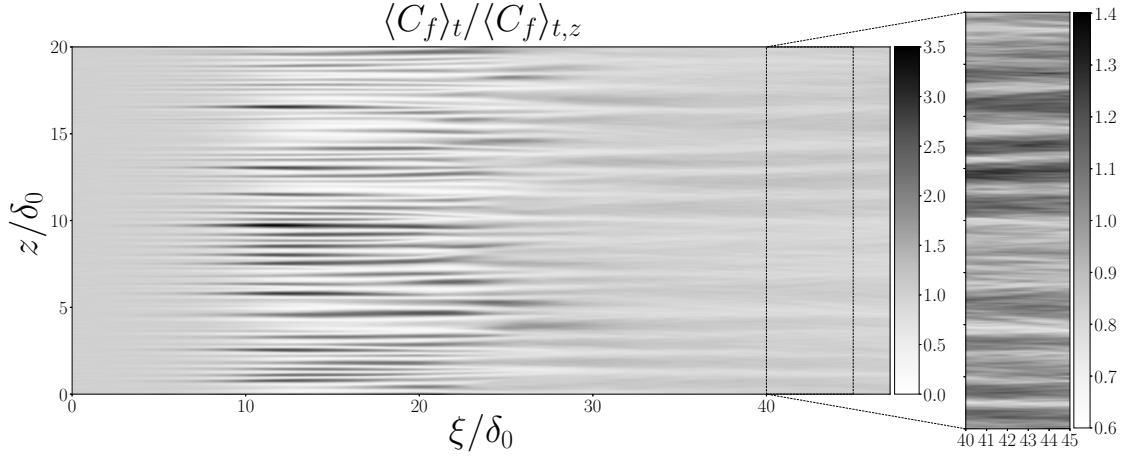


FIG. 11. Curved wall colored by the mean skin friction coefficient $\langle C_f \rangle_t$ normalized by the local spanwise averaged skin friction coefficient $\langle C_f \rangle_{t,z}$. The zoomed area in the inset ($40 < \xi / \delta_0 < 45$) highlights the persistence of the heterogeneity in the fully turbulent region.

converge and can be predicted using laminar LSA even in the fully turbulent region using the turbulent Görtler number instead of the classical G_θ .

C. Skin friction coefficient

The presence of dominant wavelengths is expected to have an effect on several properties of the flow, especially on the mean wall shear stress $\langle \tau_w \rangle_t = \mu \partial_\psi \langle u \rangle_t |_{\psi=0}$ or in its non-dimensional form, the mean skin friction coefficient $\langle C_f \rangle_t = \langle \tau_w \rangle_t / (0.5 \rho U_\infty^2)$.

In figure 11, we show the distribution of $\langle C_f \rangle_t$ over the full computational domain normalized with the spanwise-averaged skin friction coefficient $\langle C_f \rangle_{t,z}$ in order to assess the heterogeneity of the friction in the spanwise direction. The development of the Görtler instability clearly leads to a steady spanwise heterogeneity of $\langle C_f \rangle_t$ within the linear and non-linear regions ($2 < \xi / \delta_0 < 22$), as also reported in previous studies^{12–15,20,22}. In our study however, this heterogeneity clearly persists also in the turbulent region as highlighted by the inset box in figure 11 ($40 < \xi / \delta_0 < 45$). The spanwise fluctuations of $\langle C_f \rangle_t$ grow in the linear and non-linear regions ($2 < \xi / \delta_0 < 22$) up to 3.5 times the local spanwise-average $\langle C_f \rangle_{t,z}$, and up to 1.4 times in the transitional and turbulent regions ($\xi / \delta_0 > 22$), i.e. up to 40% of $\langle C_f \rangle_{t,z}$.

The phase-based statistical treatment given in equation (11) is also applied to the skin friction coefficient $\langle C_f \rangle_t$. Figure 12(a) shows the evolution of the mean skin friction coefficient $\langle C_f \rangle_{t,z}$

Linear to turbulent Görtler instability transition

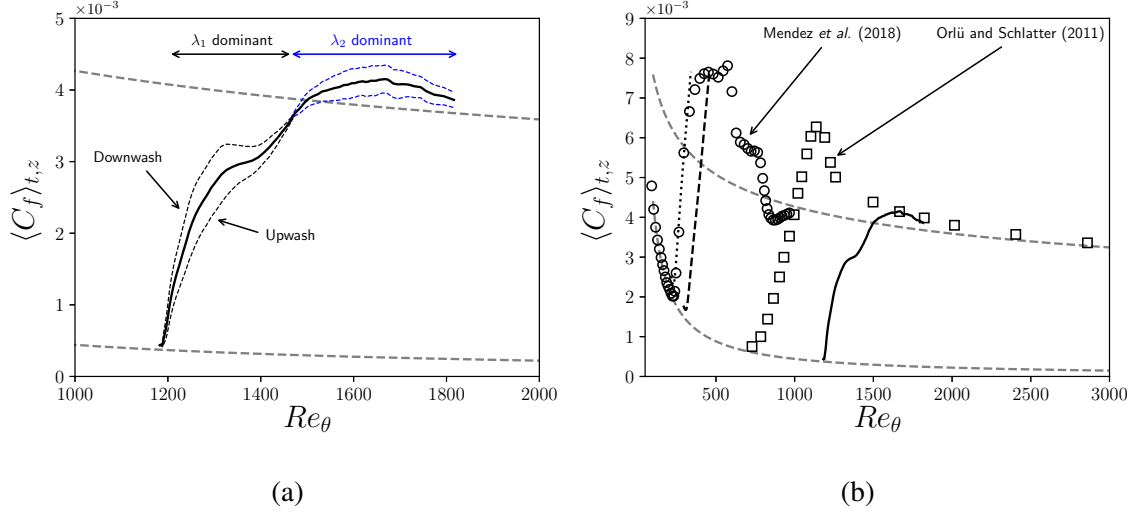


FIG. 12. (a) Evolution of the spanwise-averaged mean skin friction coefficient $\langle C_f \rangle_{t,z}$ (black solid line) and the local mean skin friction coefficient $\langle C_f \rangle_t$ at upwash (lower line) and downwash (upper line) locations with respect to λ_1 (black dashed lines) and λ_2 (blue dashed lines), as a function of Re_θ . Grey dashed lines represent theoretical laminar ($C_f = 0.441 Re_\theta^{-1}$) and turbulent ($C_f = 0.024 Re_\theta^{-1/4}$) laws, respectively, from Smits, Matheson, and Joubert³³. (b) Comparison with existing data (circles Méndez *et al.*²⁰ $Re_{\theta_0} = 75$; squares Örlü and Schlatter²³ $Re_{\theta_0} = 750$) and LES simulations at lower Re_{θ_0} and G_0 (dashed black line for $(Re_{\theta_0}, G_{\theta_0}) = (210, 13.4)$ and dotted black line for $(Re_{\theta_0}, G_{\theta_0}) = (290, 18.4)$)

(thick solid line) as a function of the Reynolds number Re_θ . Laminar and turbulent laws from Smits, Matheson, and Joubert³³ (dashed grey lines) are also reported for comparison. The evolution of $\langle C_f \rangle_t$ at upwash and downwash locations is computed using the reduced streamwise velocity field $\tilde{u}(\xi, \psi, \tilde{z})$. Upwash and downwash locations are defined with respect to the two dominant wavelengths λ_1 and λ_2 represented in figure 12 as dotted lines. The skin friction coefficient $\langle C_f \rangle_{t,z}$ detaches quickly from the laminar solution at the inflow (lower black dashed line) due to the high initial imposed Reynolds number $Re_{\theta,0} = 1,175$. In the linear region ($1175 < Re_\theta < 1220$), with the dominant wavelength λ_1 , upwash and downwash effects start to appear. In the following non-linear region, $\langle C_f \rangle_{t,z}$ upwash and downwash effects both increase noticeably. When saturation occurs, upwash and downwash effects slowly diminish, and $\langle C_f \rangle_t$ is found to be homogeneous with respect to λ_1 .

The rapid onset of the second dominant wavelength λ_2 after ceasing of λ_1 , induces a non-homogeneous distribution of $\langle C_f \rangle_t$ in both the transition and turbulent regions. Upwash and downwash effects with respect to λ_2 start to appear right after the transition to turbulence, at

Linear to turbulent Görtler instability transition

$Re_\theta = 1,500$, and do not vanish within the limits of the present computational domain. The values of $\langle C_f \rangle_{t,z}$ approach and slightly exceed the predictions for the turbulent boundary layer over a flat plate³³ in the final part of the computational domain (figure 12).

This is very different from what has been reported before^{7,13,14,20} at lower Reynolds Re_θ and Görtler G_θ numbers. In those studies, the spanwise-averaged skin friction coefficient $\langle C_f \rangle_{t,z}$ in the non-linear region clearly overshoots the theoretical predictions for a turbulent boundary layer over a flat plate and the skin friction coefficient is found to be larger already in the transition region corresponding to the domain of existence of the first unstable mode λ_1 . Here, $\langle C_f \rangle_{t,z}$ slightly exceeds the turbulent prediction only for the second dominant wavelength of the Görtler instability in the turbulent domain, as shown in figure 12a. We compare our results with those of Méndez *et al.*²⁰, Örlü and Schlatter²³ that are represented as squares and circles in figure 12(b), respectively. We also report results from additional two simulations we performed in which we fixed the initial Reynolds number $Re_\theta = 210$ (light grey line) and $Re_\theta = 290$ (dark grey line), keeping all other conditions identical. Our results at lower initial Re_θ follow those of Méndez *et al.*²⁰ and we also report an overshoot of the skin friction coefficient for the first dominant wavelength (cf. also Ducoin, Shadloo, and Roy⁷).

The high value of initial Re_θ induce non-linear effects that act primarily on smaller wavelengths, i.e. on the first appearing Görtler wavelength λ_1 . This induces a fast damping of the wavelength λ_1 resulting in a different behaviour for the skin friction coefficient C_f , where an overshoot of the turbulent plate prediction is not observed for the first appearing unstable Görtler wavelength. The results of Örlü and Schlatter²³ for large initial Re_{θ_0} report an overshoot of C_f during transition to turbulence. Here, the rapid onset of the second wavelength λ_2 allows C_f continuing increasing until it reaches and slightly exceeds the flat plate turbulent prediction, while approaching the flat plate turbulent law at the end of the computational domain.

Besides the different effects induced by initial conditions (such as tripping methods), the presence of an overshoot for the skin friction coefficient C_f appears to depend on the curvature $\sqrt{\theta/R}$ for a fixed value of the Görtler number G_θ , as reported in Méndez *et al.*²⁰: they observed a diminution of the overshoot of C_f at a given Görtler number when the radius of curvature R was increased.

IV. SUMMARY AND CONCLUSIONS

A Large Eddy Simulation of a boundary layer flow over a concave wall has been performed using a Blasius inflow profile and without turbulence and wavelength forcing. The inlet Reynolds and Görtler numbers are $Re_{\theta_0} = 1,175$ and $G_{\theta_0} = 75$, respectively. Transition to turbulence is induced by the natural development of the Görtler instability, and a developed turbulent region is reached at the end of the computational domain, with maximum $Re_{\theta} = 1,800$ and $G_{\theta} = 140$.

The developed flow over a concave wall exhibits steady large scale vortical structures that induce a spanwise heterogeneity of the mean flow properties even in the developed turbulent region, with a first clear wavelength in the initial development region $\lambda_1 = 0.385\delta_0$ and a second clear wavelength $\lambda_2 = 1.55\delta_0$ in the turbulent region.

The predictions of both the most amplified wavelength along with the associated spatial modes obtained by extending the LSA of Floryan and Saric³ to a wider parameter domain of G_{θ} and the non-dimensional wavelength Λ well compare to the computed wavelength and the spanwise averaged spatial modes in the linear region for λ_1 . The dominant wavelength λ_2 in the turbulent domain is well predicted with the LSA if a turbulent Görtler number is considered, in which the kinematic viscosity ν is replaced by the turbulent viscosity ν_t , as proposed by Tani¹¹. Also, the spatial modes associated with λ_2 converge with a low scatter in the turbulent region.

The skin friction coefficient $\langle C_f \rangle_t$ increases locally up to a factor 3.5 in the non-linear region of dominance of λ_1 and up to a factor of 1.4 in the developed turbulent region for the downwash location of the λ_2 Görtler instability, very different from the homogeneous distribution of $\langle C_f \rangle_t$ reported previously in the literature, in which no Görtler vortices develop in the turbulent region because the estimated turbulent Görtler number is close or even below the neutral stability curve. Thus, the flow in the turbulent region becomes Görtler stable. The high value of initial Re_{θ} induce non-linear effects that act primarily on the first appearing Görtler wavelength λ_1 damping its growth, so that the skin friction coefficient C_f slightly exceeds the flat plate turbulent prediction for the second dominant wavelength λ_2 at the end of the computational domain, and no overshoot of C_f is reported in the region of dominance of λ_1 . Additional simulations we performed with a smaller initial $Re_{\theta,0}$ are in accord with previous studies with an overshoot of C_f for the first dominant Görtler wavelength with respect to the turbulent plate predictions.

ACKNOWLEDGMENTS

This work has been supported by a grant from Labex OSUG (Investissements d’avenir – ANR10 LABX56). V. Moureau and G. Lartigue (CORIA), and the SUCCESS scientific group are acknowledged for providing the YALES2 code. This work was granted access to the HPC resources of IDRIS under the allocation 2019-A0060107567 made by GENCI.

Special thanks go to E.J. Hopfinger for fruitful discussions.

DATA AVAILABILITY STATEMENT

The data that support the findings of this study are available from the corresponding author upon reasonable request.

REFERENCES

- ¹H. Görtler, “Über eine dreidimensionale Instabilität laminarer Grenzschichten an konkaven Wänden,” *Nachr. Ges. Wiss. Göttingen*, NF **2**, 1–26 (1940).
- ²A. Smith, “On the growth of taylor-görtler vortices along highly concave walls,” *Quart. App. Math.* **13**, 233–262 (1955).
- ³J. Floryan and W. Saric, “Stability of görtler vortices in boundary layers,” *AIAA journal* **20**, 316–324 (1982).
- ⁴P. Hall, “The linear development of görtler vortices in growing boundary layers,” *J. Fluid Mech.* **130**, 41–58 (1983).
- ⁵W. Saric, “Görtler vortices,” *Ann. Rev. Fluid Mech.* **26**, 379–409 (1994).
- ⁶S. Navarro-Martinez and O. Tutty, “Numerical simulation of görtler vortices in hypersonic compression ramps,” *Comp. & Fluids* **34**, 225–247 (2005).
- ⁷A. Ducoin, M. Shadloo, and S. Roy, “Direct numerical simulation of flow instabilities over savonius style wind turbine blades,” *Ren. Ener.* **105**, 374–385 (2017).
- ⁸E. Hopfinger, A. Kurniawan, W. Graf, and U. Lemmin, “Sediment erosion by görtler vortices: the scour-hole problem,” *J. Fluid Mech.* **520**, 327–342 (2004).
- ⁹I. Albayrak, E. Hopfinger, and U. Lemmin, “Near-field flow structure of a confined wall jet on flat and concave rough walls,” *J. Fluid Mech.* **606**, 27–49 (2008).

- ¹⁰C. Brun, “Large-eddy simulation of a katabatic jet along a convexly curved slope: 2. evidence of görtler vortices,” *J. Geophys. Res. Atm.* **122**, 5190–5210 (2017).
- ¹¹I. Tani, “Production of longitudinal vortices in the boundary layer along a concave wall,” *J. Geophys. Res.* **67**, 3075–80 (1962).
- ¹²J. Swearingen and R. Blackwelder, “The growth and breakdown of streamwise vortices in the presence of a wall,” *J. Fluid Mech.* **182**, 255–290 (1987).
- ¹³T. Tandiono, S. Winoto, and D. Shah, “Spanwise velocity component in nonlinear region of görtler vortices,” *Phys. of Fluids* **25**, 104104 (2013).
- ¹⁴L.-U. Schrader, L. Brandt, and T. Zaki, “Receptivity, instability and breakdown of görtler flow,” *J. Fluid Mech.* **682**, 362–396 (2011).
- ¹⁵V. Malatesta, L. Souza, and J. Lui, “Influence of goertler vortices spanwise wavelength on heat transfer rates,” *Comp. Therm. Sci.* **5**, 389–400 (2013).
- ¹⁶L. Souza, “On the odd and even secondary instabilities of görtler vortices,” *Theoretical and Computational Fluid Dynamics* **31**, 405–425 (2017).
- ¹⁷M. B. J. M. P. A. N. H. M. S. A. J. Marusic, I. and K. R. Sreenivasan, “Wall-bounded turbulent flows at high reynolds numbers: Recent advances and key issues.” *Phys. Fluids* , 065103 (2010).
- ¹⁸P. Schlatter, Q. Li, G. Brethouwer, A. Johansson, and D. Henningson, “Structure of a turbulent boundary layer studied by dns,” in *Direct and Large-Eddy Simulation VIII* (Springer, 2011) pp. 9–14.
- ¹⁹P. Schlatter and R. Örlü, “Inflow length and tripping effects in turbulentboundary layers,” *J. Phys.: Conf. Ser.* **318**, 022018 (2011).
- ²⁰M. Méndez, M. Shadloo, A. Hadjadj, and A. Ducoin, “Boundary layer transition over a concave surface caused by centrifugal instabilities,” *Computers & Fluids* **171**, 135–153 (2018).
- ²¹D. Park and P. Huerre, “Primary and secondary instabilities of the asymptotic suction boundary layer on a curved plate,” *J. Fluid Mech.* **283**, 249–272 (1995).
- ²²M. Schultz and R. Volino, “Effects of concave curvature on boundary layer transition under high freestream turbulence conditions,” *J. Fluids Eng.* **125**, 18–27 (2003).
- ²³R. Örlü and P. Schlatter, “Inflow length and tripping effects in turbulent boundary layers,” in *Journal of Physics: Conference Series*, Vol. 318 (IOP Publishing, 2011) p. 022018.
- ²⁴V. Moureau, P. Domingo, and L. Vervisch, “Design of a massively parallel cfd code for complex geometries,” *Comptes Rendus Mécanique* **339**, 141 – 148 (2011), *high Perf. Comp.*

- ²⁵A. Chorin, “Numerical solution of the navier-stokes equations,” *Math. of Comp.* **22**, 745–762 (1968).
- ²⁶M. Malandain, N. Maheu, and V. Moureau, “Optimization of the deflated conjugate gradient algorithm for the solving of elliptic equations on massively parallel machines,” *J. Comp. Phys.* **238**, 32 – 47 (2013).
- ²⁷M. Germano, U. Piomelli, P. Moin, and W. Cabot, “A dynamic subgrid-scale eddy viscosity model,” *Phys. of Fluids* **3**, 1760–1765 (1991).
- ²⁸I. Orlanski, “A simple boundary condition for unbounded hyperbolic flows,” *Journal of computational physics* **21**, 251–269 (1976).
- ²⁹S. B. Pope, “Turbulent flows,” (2001).
- ³⁰P. Benard, G. Balarac, V. Moureau, C. Dobrzynski, G. Lartigue, and Y. D’Angelo, “Mesh adaptation for large-eddy simulations in complex geometries,” *International Journal for Numerical Methods in Fluids* **81**, 719–740 (2016).
- ³¹P. Petitjeans, *Étude expérimentale des instabilités de couches limites sur des parois concaves : Instabilité de Görtler*, Phd thesis (1992).
- ³²F. H. Clauser, “The turbulent boundary layer,” *Adv. Appl. Mech.* **4**, 1–51 (1956).
- ³³A. Smits, N. Matheson, and P. Joubert, “Low-reynolds-number turbulent boundary layers in zero and favorable pressure gradients,” *Journal of ship research* **27**, 147–157 (1983).